Unveiling Intrinsic Bulk Photovoltaic Effect in Atomically Thin ReS$_2$

Maria Ramos,* Tanweer Ahmed, Bao Q. Tu, Eleni Chatzikyriakou, Lucía Olano-Vegas, Beatriz Martín-García, M. Reyes Calvo, Stepan S. Tsirkin, Ivo Souza, Félix Casanova, Fernando de Juan, Marco Gobbi,* and Luis E. Hueso*

ACCESS | Metrics & More | Article Recommendations | SI Supporting Information

ABSTRACT: The bulk photovoltaic effect (BPVE) offers a promising avenue to surpass the efficiency limitations of current solar cell technology. However, disentangling intrinsic and extrinsic contributions to photocurrent remains a significant challenge. Here, we fabricate high-quality, lateral devices based on atomically thin ReS$_2$ with minimal contact resistance, providing an optimal platform for distinguishing intrinsic bulk photovoltaic signals from other extrinsic photocurrent contributions originating from interfacial effects. Our devices exhibit large bulk photovoltaic performance with intrinsic responsivities of ∼1 mA/W in the visible range, without the need for external tuning knobs such as strain engineering. Our experimental findings are supported by theoretical calculations. Furthermore, our approach can be extrapolated to investigate the intrinsic BPVE in other noncentrosymmetric van der Waals materials, paving the way for a new generation of efficient light-harvesting devices.

KEYWORDS: bulk photovoltaics, intrinsic photocurrent, second-order conductivity, broken inversion symmetry
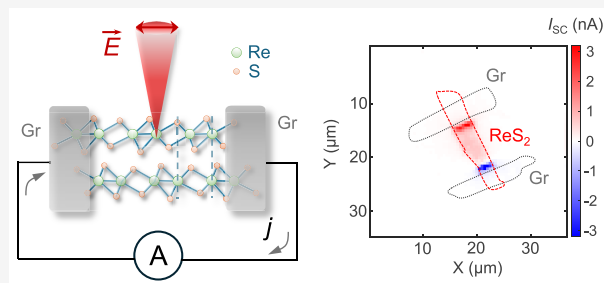
The exploitation of high-order, nonlinear photocurrents could potentially overcome the fundamental efficiency limit of current solar cells based on p-n junctions.[1−3] This limit, known as the Shockley-Queisser limit, is directly related to the active material's bandgap. It dictates a maximum theoretical efficiency of about 33.7% for a single junction under standard conditions.[4,5] While multijunction solar cells can achieve higher efficiencies, they remain restricted by the bandgaps of their constituent materials, limiting the utilization of lower-energy parts of the spectrum. Nonlinear photocurrents, unconstrained by bandgap limitations, present a feasible alternative to unlock the full potential of the solar spectrum and surpass the efficiency limit, extending light utilization into the infrared and beyond.[6−9]

The proportionality relation between second-order photocurrents and an applied electric field (or light polarization) in a material is dictated by the nonlinear conductivity tensor $\sigma^{(2)}$, which is determined by the material's symmetry. Breaking inversion symmetry is essential for the emergence of second-order photocurrents, leading to what is commonly referred to as "bulk" photovoltaic effect (BPVE). These terms reflect the characteristics of this phenomenon: the generation of a net DC photocurrent upon illumination of a single, homogeneous material at zero applied bias.

While the discovery of the BPVE originated from research on ferroelectric perovskite oxides,[10−17] these materials have not been considered a viable solution against traditional solar cell technology due to their low light-to-electrical power conversion efficiency. Alternatively, van der Waals (vdW)

materials present straightforward strategies for breaking inversion symmetry, offering a new and exciting avenue for BPVE research.[18−28] Especially, vdW polar materials have demonstrated large responsivities on the order of 1−10 mA/W when implemented in vertical device architectures.[29−33]

Among various promising vdW materials, ReS$_2$ emerges as a particularly attractive candidate for BPVE exploration. While bulk ReS$_2$ is centrosymmetric,[34,35] numerous studies highlighted the polytypism in the material.[36,37] Different stacking orders of the distorted 1T crystal structure (known as 1T') can lead to broken symmetries, particularly in the few-layer limit of ReS$_2$ where stacking energetics can differ from that of bulk samples. This broken symmetry is crucial for the emergence of several nonlinear phenomena such as second harmonic generation (SHG), as demonstrated by Song et al.,[38] and ferroelectricity, as confirmed by Wan et al.[39] in few-layer ReS$_2$. These findings suggest the potential for a significant BPVE in few-layer ReS$_2$. Earlier reports on BPVE in ReS$_2$ have observed photocurrents at zero applied bias only at grain boundaries in polycrystalline flakes,[40] or solely at the crystalline edge of heterostructures formed by two ReS$_2$ flakes.[41] Furthermore,
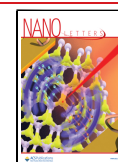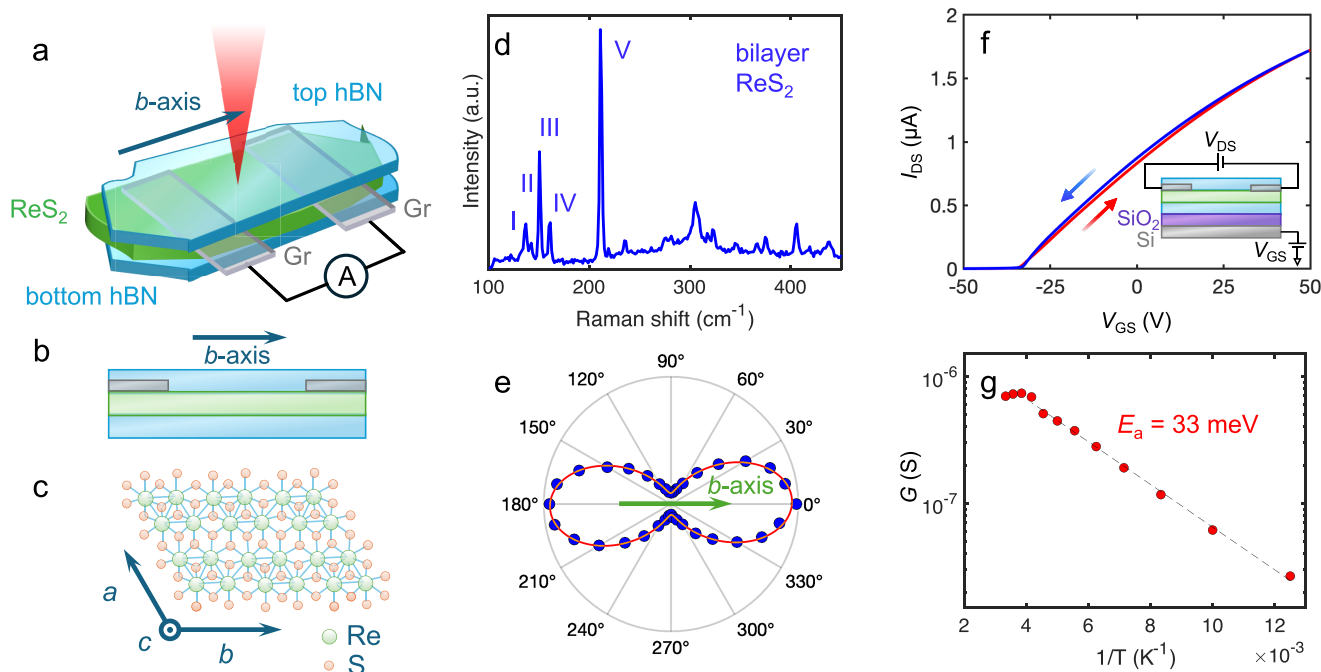
Figure 1. Simplified three-dimensional (a) and cross-sectional (b) device schemes showing the different vdW layers composing the system. The color coding chosen for each material layer in panel b is the same as for panel a. In panel a, a CW (continuous wave) laser is used to illuminate the device, while a current meter reads the photogenerated current. (c) Top-view atomic configuration of a monolayer ReS_2 with 1T′ structure. (d) Raman spectrum of a bilayer ReS_2, where the first five vibrational modes can be clearly identified. (e) Polar plot of the A_g-like active Raman mode at ∼212 cm^{-1} (mode V in panel d). The orientation of the Re−Re bonds (b-axis) is identified along the maximum intensity. (f) Back- and forth-transfer curves of one of the fabricated devices, upon back-gate voltage (see sketch in the inset) and in dark conditions for V_{DS} = 0.2 V. (g) Arrhenius plot for the conductance, where a linear fit to the data yields an activation energy of 33 meV.

Wang et al.[42] reported BPVE in single-crystalline ReS_2 flakes using a vertical device geometry.

Nonetheless, vertical geometries face challenges in the identification of the intrinsic BPVE. A key challenge in BPVE research lies in distinguishing nonlinear photocurrents from those generated at Schottky barriers within a device. This differentiation is crucial, as the Schottky barrier photovoltaic effect can dominate the overall photocurrent, questioning whether the responsivity has an intrinsic origin. Lateral geometries with a focused incoming beam enable spatial separation of intrinsic and extrinsic effects, facilitating detection of photocurrents from the pristine, active material without ambiguity. However, sizable BPVE signals under normal incidence excitation in lateral devices using non-centrosymmetric transition metal dichalcogenides usually require the application of external tuning knobs, such as strain.[43,44]

In this work, we overcome the limitations found across the literature by employing an optimal device engineering technique, which enables to clearly identify the BPVE in thin, single-crystalline ReS_2 flakes without the need of external tuning knobs or vertical device architectures. Our approach utilizes a lateral device geometry where the ReS_2 layer is in contact with graphite electrodes and encapsulated between hexagonal boron nitride (hBN). This yields devices with minimal contact resistance, reducing electrode-interface photo-currents and providing an optimal platform for sensitive detection of intrinsic nonlinear photocurrents. We demonstrate the BPVE in ReS_2 by studying the dependence of the observed photocurrent on the incoming light polarization and

its spatial distribution across the device. Remarkably, our approach enables the detection of a large BPVE response in ReS_2, with intrinsic responsivities of ∼ 1mA/W. These experimental values are seconded by our calculated photo-current response based on a noncentrosymmetric bilayer structure. Additionally, our fabrication approach can poten-tially be extrapolated to the study of the BPVE in other noncentrosymmetric vdW materials with no perpendicular 2-fold rotational axis, where in-plane photocurrents are generically allowed even at normal incidence.

A critical aspect of successfully measuring a BPVE signal is employing a device design that minimizes unwanted effects and maximizes the contribution of the "intrinsic", active material. To achieve this, we employ a device fabrication with the following considerations: First, a lateral device geometry is chosen to separate the BPVE from other potential photovoltaic effects originating at interface between different materials, which are typically present in devices with vertical geometries. Second, the ReS_2 active layer is sandwiched in between two thin hBN flakes to minimize surface defects and prevent any influence from the substrate. Third, few-layer graphite flakes are used as electrodes in contact with ReS_2 to minimize contact resistance. Fourth, a pick-up technique is employed during the device assembly to ensure clean interfaces between all materials. Further details about device fabrication are provided in Section S1.

Figure 1a-b summarizes the different vdW layers present in the devices through simplified sketches from both 3D and cross-sectional viewpoints, respectively. A bilayer-thick ReS_2 flake serves as the active channel, contacted by two thin
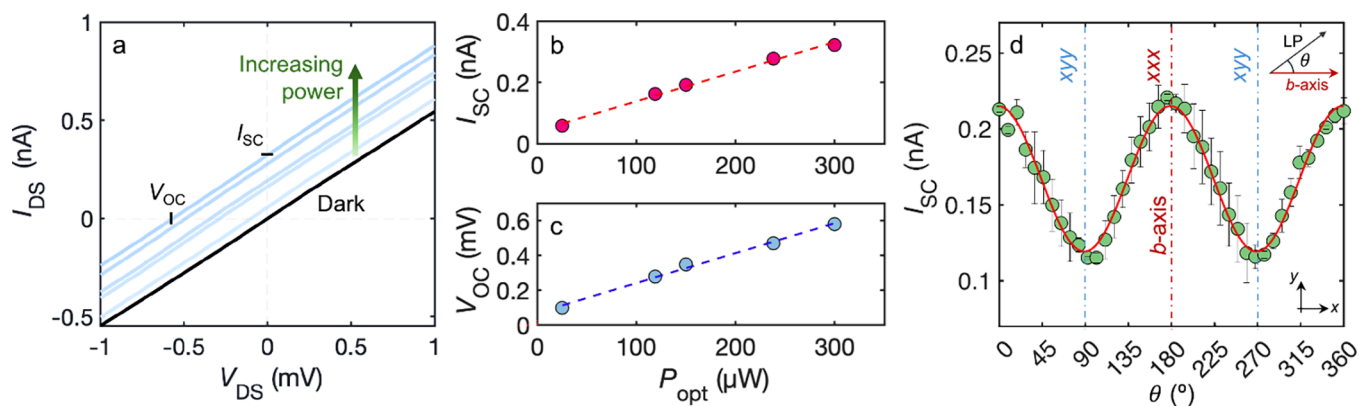
Figure 2. (a) $I_{DS}-V_{DS}$ characteristics of the ReS$_2$ device in the dark and upon illumination powers from 30 to 300 μW at 633 nm wavelength. (b) Short-circuit current extracted from panel a. (c) Open-circuit voltage obtained from panel a. (d) Angular dependence of the short-circuit current measured along the b-axis as a function of the linear polarization of the incoming light. The top right inset indicates the relative angle θ between the crystallographic b-axis of ReS$_2$ and the linear polarization of light (LP). Here, the b-axis is aligned with the x-coordinate (this happens at $\theta = 0°$, $180°$, $360°$). Measurements are carried out with an excitation wavelength of 633 nm for an optical power of 120 μW.

graphite electrodes and encapsulated between top and bottom hBN flakes (see Section S2 for ReS$_2$ thickness estimation). The vdW stack illustrated in Figure 1a-b is placed onto a SiO$_2$/Si^{2+} substrate.

The top-view atomic configuration of a monolayer ReS$_2$ with 1T' structure is shown in Figure 1c, where Re-Re bonds form chains along the b-axis. The unit cell of ReS$_2$ contains four rhenium atoms and eight sulfur atoms, with the a and b axes forming an angle of 118°.[34,35] As indicated in panels a and b of Figure 1, current detection is carried out along the b-axis of the ReS$_2$ flakes, as the crystals are naturally cleaved along this crystallographic direction. This is also confirmed through polarization-resolved Raman spectroscopy of the vibrational mode V ($\sim$212 cm^{-1}). As mode V involves out-of-plane vibrations of S atoms coupled with in-plane vibrations of Re atoms along the b-axis, a beam polarized along the direction of the Re atomic chain optimally couples with the in-plane vibrational component of the V mode. Consequently, the polarization at which the intensity of mode V is maximum indicates the orientation of the b-axis (see Figure 1d-e).

To ensure the quality and functionality of the fabricated devices, we check the transfer characteristics of a representative device (see Figure 1f). These measurements reveal a well-defined on/off switching ratio of $\sim 10^3$ and a field-effect mobility of 12 cm^2/(V·s), indicating good quality and efficient carrier transport in agreement with previous reports.[45] In addition, the transfer curves exhibit very small hysteresis, suggesting minimal charge trapping effects within the device.

Low contact resistance is essential for detecting second-order photocurrents. Our graphite electrodes minimize Schottky barriers, enabling efficient carrier extraction. This is confirmed by the low activation energy of our device, $E_a = 33$ meV (see Figure 1g), significantly lower than ReS$_2$ devices contacted to traditional metals.[46,47]

With the optimized ReS$_2$ devices in hand, we next investigate their intrinsic photovoltaic response. To do this, different $I_{DS}-V_{DS}$ curves in dark conditions and under illumination are studied. During the measurement, a linearly polarized laser emitting at 633 nm is used to illuminate the ReS$_2$ channel at different excitation powers. To avoid any photocurrent contribution from the ReS$_2$/graphite interface, the laser beam is tightly focused to a ~ 1 μm spot size onto the center of the ReS$_2$ channel, whose length exceeds 5 μm.

The current–voltage characteristics shown in Figure 2a under dark conditions follow a linear trend, evidencing low contact resistance (see Section S3 for larger applied voltages). Upon illumination, the $I_{DS}-V_{DS}$ curves exhibit a significant displacement that increases with the optical excitation power. This displacement indicates the generation of photocurrent at zero applied bias (short-circuit current, I_{SC}) and a nonzero voltage at zero current (open-circuit voltage, V_{OC}). These parameters define the operating regime of the device under illumination, where light-to-electrical power conversion occurs.

The values of the short-circuit current and the open-circuit voltage from Figure 2a are shown respectively in Figure 2b-c as a function of the excitation power. Both I_{SC} and V_{OC} exhibit a linear dependence on the excitation power (P_{opt}). This is indicative of a second-order photocurrent generation process, since power scales proportionally to the square of the electric field ($P_{opt} \propto |E|^2$).

A characteristic feature of a BPVE current is its sensitivity to the linear polarization of the incident light, whose response can be understood from the nonlinear conductivity σ^2 describing the material's response. To investigate this, we measured the short-circuit current at different angles of the linearly polarized light with respect to the b-axis of ReS$_2$. The results are shown in Figure 2d, where the green dots represent the experimental data and the error bars indicate the standard deviation for each measurement. The results confirm a strong correlation between the short-circuit current and the light polarization, with a photocurrent approximately 2× larger when the light polarization aligns with the b-axis of ReS$_2$.

Interestingly, while the photocurrent exhibits a clear periodic modulation with light polarization, it remains nonzero for any polarization orientation. This agrees with previous observations of nonvanishing SHG for all polarization angles in ReS$_2$[38] since these two effects are determined by the inherent crystal symmetry of ReS$_2$. Moreover, the nonzero mean photocurrent reveals a polar nature for ReS$_2$ crystals.

The results in Figure 2d can be described by an equation capturing the relationship between a second-order photocurrent density along a given i-direction and the nonlinear conductivity tensor as a quadratic electric field response:

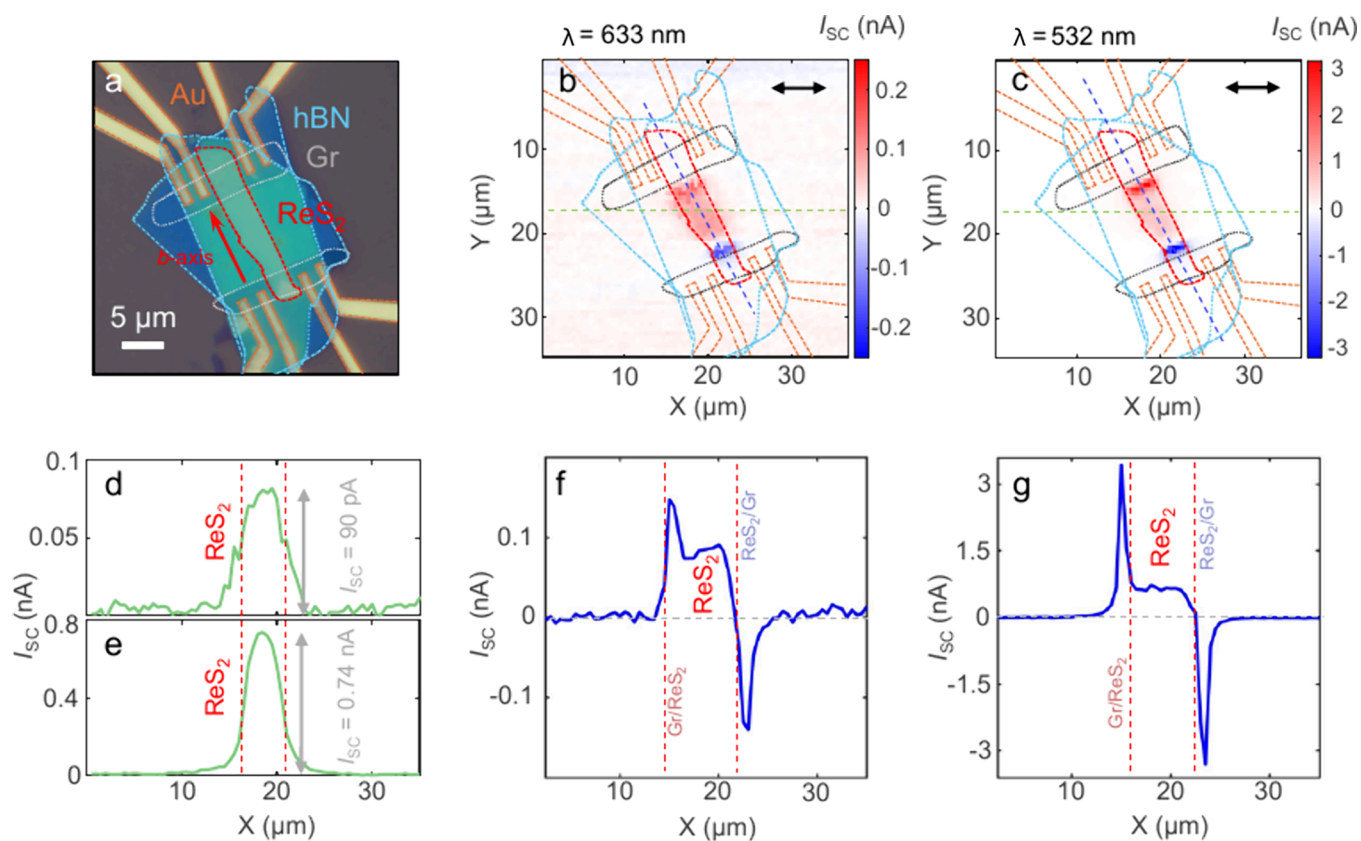$$j_i^{BPVE} = \sigma_{ijk}^{(2)} E_j E_k \tag{1}$$

Figure 3. (a) Optical microscope image of a ReS$_2$ device. (b, c) Scanning photocurrent maps of the device shown in panel a for excitation wavelengths of 633 and 532 nm at excitation powers of 30 μW and 400 μW, respectively. The color scale represents the photocurrent intensity, with red and blue colors indicating positive and negative photocurrents, respectively. The black, double arrows at the top, right-hand side indicate the orientation of the linear polarization of light. (d, e) Transverse line profiles obtained from the photocurrent maps shown in panels b and c, respectively. (f, g) Longitudinal line profiles extracted from the photocurrent maps in panels b and c, respectively, where the reddish and bluish areas indicate positive and negative photocurrents built at the lateral Schottky barriers between the active channel and the graphite contacts.

where $\sigma_{ijk}^{(2)}$ is the second-order conductivity and E_j, E_k are the components of the applied electric field along j and k, which in our case correspond to the electric field direction of the incoming light wave (or light polarization).

Since photocurrent is directly measured during experiments, from here onward we provide the equations in terms of total photocurrent (I) and not photocurrent density (j). In our experiments, both the electric field (or light polarization) and the photocurrent detection are restricted to an in-plane configuration. Consequently, tensor components like those describing current flow along the z-axis can be disregarded. Also, since the photocurrent detection takes place along the b-axis of ReS$_2$, we adopt a convention where the b-axis aligns with the x-coordinate direction of our experimental setup. Therefore, the equation describing the photocurrent simplifies to:

$$I_x = t \cdot r (\sigma_{xxx}^{(2)} E_x^2 + \sigma_{xyy}^{(2)} E_y^2 + 2\sigma_{xxy}^{(2)} E_x E_y) \quad (2)$$

where t is the ReS$_2$ thickness and r is the beam radius. Considering an electric field amplitude E_0 forming an angle θ with respect to the x-axis, the electric field components can be written as $E_x = E_0 \cos \theta$ and $E_y = E_0 \sin \theta$. For a Gaussian beam, the electric field amplitude can be written in terms of optical power as $E_0^2 = 4P_{opt}/(nc\varepsilon_0 \pi r^2)$, where n is the refractive index of ReS$_2$, c is the speed of light and ε_0 is the vacuum permittivity. Substituting these expressions into eq. 2, the photocurrent as a function of the polarization angle becomes:

$$I_x = 4\frac{t \cdot P_{opt}}{n\pi c\varepsilon_0 r}(\sigma_{xxx}^{(2)} \cos \theta^2 + \sigma_{xyy}^{(2)} \sin \theta^2 + 2\sigma_{xxy}^{(2)} \cos \theta \sin \theta)$$

$$(3)$$

A fit of the polarization dependent photocurrent in Figure 2d using eq. 3 yields nonlinear conductivity values of $\sigma_{xxx}^{(2)} = (5.51 \pm 0.07)$ μA/V^2, $\sigma_{xyy}^{(2)} = (3.06 \pm 0.07)$ μA/V^2 and $\sigma_{xxy}^{(2)} = (-0.05 \pm 0.06)$ μA/V^2 within a 95% confidence interval. Further details on the fitting parameters used in this analysis are provided in Section S4 of the Supporting Information.

To compare with other works, the responsivity of the device can be obtained from Figure 2d. Since the responsivity is directly influenced by the sample dimension, a normalization based on sample size is needed for accurate comparisons across different studies. The "intrinsic" responsivity of our device is calculated from Figure 2d as the ratio of the photocurrent density to the laser power density: $\kappa = (j^{BPVE}/I_{opt})$, where $j^{BPVE} = <I_{SC}>/(r \cdot t)$ and $I_{opt} = P_{opt}/(\pi \cdot r^2)$ being $<I_{SC}>$ the mean photocurrent, r the laser beam radius, t the ReS$_2$ thickness and P_{opt} the optical power. For our bilayer device, this yields a BPVE intrinsic responsivity of 1.3 mA/W.

We employed scanning photocurrent microscopy (SPCM) to detect variations in the device's photovoltaic response across different regions. Figure 3a shows an optical microscope image of a representative device with a four-layer ReS$_2$ active channel. The corresponding SPCM maps are shown in Figure 3b-c, obtained under different illumination wavelengths and
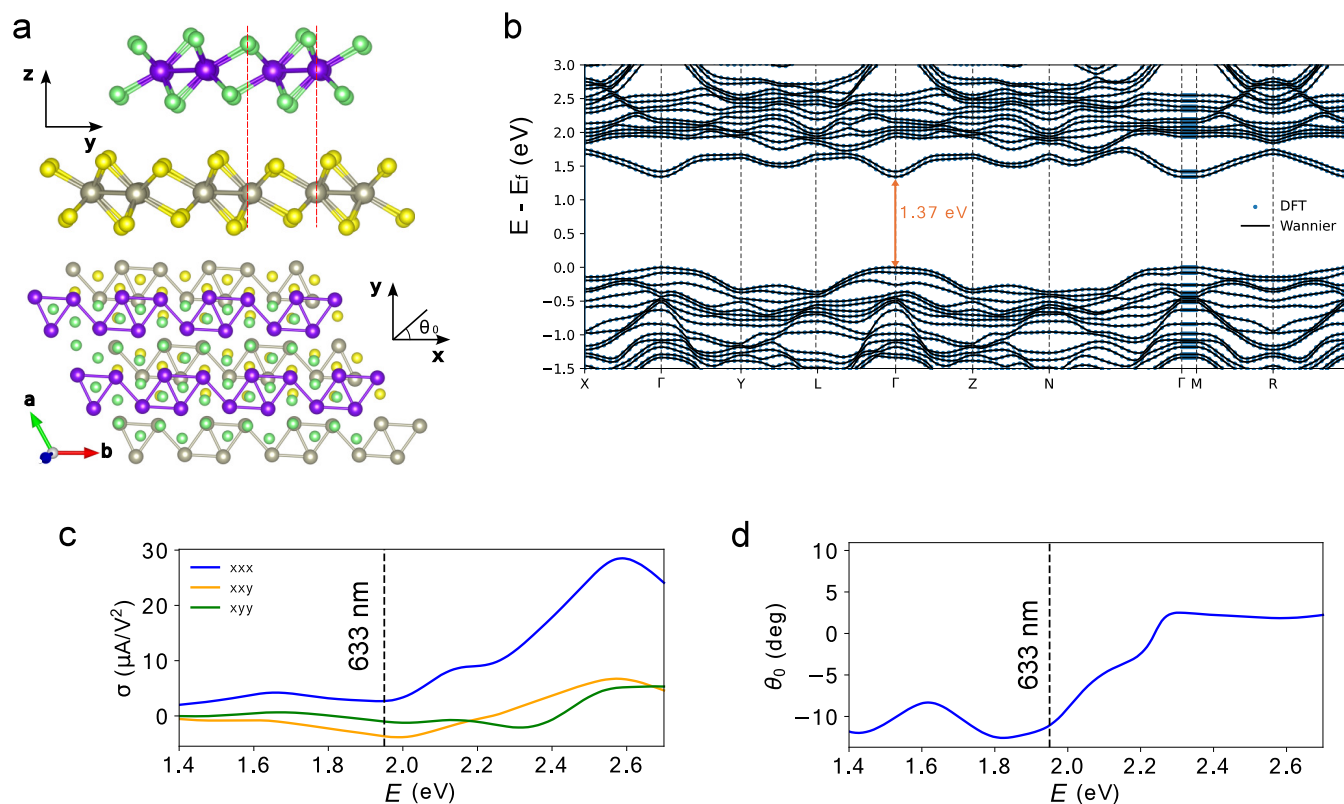
Figure 4. (a) Lattice structure of noncentrosymmetric ReS$_2$ bilayer. (b) Computed band structure comparing *ab initio* and Wannierized bands. (c) Nonlinear conductivity as a function of energy for all in-plane components. The dashed line corresponds to a laser wavelength of 633 nm (~1.95 eV) for comparison with experiment. (d) Angle of maximum photocurrent as a function of energy, which is within the range of $[-12°, +2°]$ relative to the b-axis for all the calculated energies.

excitation powers, with zero applied bias. Both SPCM maps exhibit a remarkable similarity in the spatial distribution of the photogenerated current across the ReS$_2$ device for the two excitation wavelengths. The SPCM maps show a photocurrent with opposite sign at the lateral contact regions, located at both ends of the ReS$_2$ channel. The dominant mechanism of this photocurrent is a photovoltaic effect due to a built-in electric field at the graphite/ReS$_2$ interface. Here, the source (drain) barrier drives photogenerated electrons (holes) toward the semimetal contact, resulting in a positive (negative) photocurrent. Furthermore, the SPCM maps also reveal a photocurrent generated within the ReS$_2$ channel.

The corresponding transverse profiles are respectively depicted in Figure 3d-e, displaying a distinct and sharp increase in current when the ReS$_2$ active channel is illuminated. This rise indicates efficient photocurrent generation within the ReS$_2$ channel itself and its magnitude exhibits a direct proportionality to the illumination power used for excitation.

While the transverse profiles focus on current fluctuations across the ReS$_2$ channel, the longitudinal profiles track the current along the ReS$_2$ active layer. The data obtained from the longitudinal line profiles in Figure 3f-g provides valuable insights into the different contributions to the overall photocurrent signal. A constant dark current or noise level can be identified when the device is illuminated in non-photoresponsive regions. The photocurrent built at the lateral semimetal/semiconductor interface appears at the edges of the ReS$_2$ channel with opposite sign contributions, with an extension of ~ 2-μm. Finally, in the central area of the device,

the bulk photovoltaic current generated along the ReS$_2$ channel can be distinguished.

Significantly, the longitudinal line profiles reveal a disparity in the scaling behavior between the photovoltaic current built at the lateral semimetal/semiconductor interface and that originating from the pristine ReS$_2$ flake, supporting the distinct origins of the two signals. Moreover, the magnitude of the photocurrent originated along the pristine ReS$_2$ flake in the longitudinal line profiles is consistent with the photocurrent intensity observed in the transverse line profiles. The uniformity of this signal across the SPCM maps and its sharp rise in the line profiles further support the dominance of the BPVE as the mechanism for photocurrent generation in our device.

Interestingly, we are not able to discern any BPVE signal in lateral ReS$_2$ devices fabricated with traditional metal contacts, such as prepatterned Ti/Au electrodes, as confirmed by the absence of any photocurrent at zero bias originated at the pristine ReS$_2$ channel through SPCM maps. Moreover, the Schottky barrier photocurrent is an order of magnitude greater than that observed in our graphite-contacted devices (see Section S5 of the Supporting Information).

The device characterized in Figure 3 exhibits intrinsic responsivities of 1.6 and 1.0 mA/W at wavelengths of 633 and 532 nm, respectively, for a ReS$_2$ channel containing four layers. Our low-contact-resistance devices outperform similar lateral devices characterized under analogous experimental conditions, where unstrained noncentrosymmetric 3R- and 2H-MoS$_2$ exhibited negligible BPVE currents.[43,44]

While bulk ReS_2 is centrosymmetric,[34,35] different stacking orders of the 1T' crystal structure can lead to broken symmetries in the few-layer limit. Recent works have pointed out the existence of a bilayer stacking different from the bulk one, where the top monolayer is rotated by 180° with respect to the bottom one. This generically leads to a non-centrosymmetric structure which is ferroelectric[39] and displays SHG,[48] being also expected to generate a BPVE current.

We have performed an *ab initio* calculation of the nonlinear conductivity in the noncentrosymmetric state defined in ref.,[39] using Wannier functions derived from first principles simulations[49] (see Section S1 for details).

The response tensor $\sigma_{ijk}^{(2)}$ was calculated from:

$$\sigma_{ijk}^{(2)}(0, \omega, -\omega) = -\frac{i\pi e^3}{4\hbar^2} \int [d\boldsymbol{k}] \sum_{n,m} f_{nm}(I_{mn}^{abc} + I_{mn}^{acb})$$

$$[\delta(\omega_{mn} - \omega) + \delta(\omega_{nm} - \omega)] \tag{4}$$

where I_{kmn}^{abc} is the product of the interband dipole matrix and its generalized derivative with respect to the crystal momentum, $f_{nm} = f_{n^-} f_m$ are Fermi occupation factors and $\hbar\omega_{nm} = E_m - E_n$ is the difference between the energies of bands n and m.

The results are depicted in Figure 4, where the x coordinate corresponds to the b-axis of the ReS_2 crystal and to the direction of current flow in our experiments. At 633 nm wavelength, we obtained the components $\sigma_{xxx}^{(2)} = 2.68$, $\sigma_{xyy}^{(2)} = -1.03$ and $\sigma_{xxy}^{(2)} = -3.71$ $\mu A/V^2$ (Figure 4c). Our model predicts a photocurrent with the same order of magnitude as the one observed experimentally, something noteworthy in this field.

We obtained the angle θ_0 at which photocurrent should be maximum from eq. 3 as: $\theta_0 = \frac{1}{2}\arctan 2\sigma_{xxy}^{(2)}/(\sigma_{xxx}^{(2)} - \sigma_{xyy}^{(2)})$. These results predict a maximum photocurrent at angles falling within the range of [-12°, +2°] with respect to the b-axis of ReS_2 for all the energies computed. These angles fall within an acceptable range of ± 10° angular error for our experimental setup, due to inherent limitations associated with aligning the polarization relative to the b-axis of the ReS_2 crystal.

In summary, our work unveils intrinsic BPVE in atomically thin ReS_2 through lateral device engineering. Scanning photocurrent microscopy and polarization-dependent photocurrent measurements provide compelling evidence for intrinsic photocurrent generation mechanisms. The $\sigma^{(2)}$ values extracted from experimental data are in the same order of magnitude as those obtained from theoretical calculations based on a noncentrosymmetric ReS_2 bilayer. Our device engineering strategy, combined with advanced characterization and theoretical calculations could be extended to study the intrinsic BPVE response in a broad range of noncentrosymmetric vdW materials.

■ ASSOCIATED CONTENT

ⓢ Supporting Information

The Supporting Information is available free of charge at https://pubs.acs.org/doi/10.1021/acs.nanolett.4c03944.

> Methods; thickness estimation of ReS_2 active layers; $I_{SD}-V_{SD}$ characteristics up to 1 V; estimation of nonlinear conductivity from polarization-dependent photocurrent measurements; scanning photocurrent microscopy of a ReS_2 device with Ti/Au electrodes (PDF)

■ AUTHOR INFORMATION

Corresponding Authors

Maria Ramos − CIC nanoGUNE BRTA, 20018 Donostia-San Sebastián, Basque Country, Spain; ⓞ orcid.org/0000-0001-7701-5911; Email: m.ramos@nanogune.eu

Marco Gobbi − Centro de Física de Materiales CSIC-UPV/EHU, 20018 Donostia-San Sebastián, Basque Country, Spain; IKERBASQUE, Basque Foundation for Science, 48009 Bilbao, Basque Country, Spain; ⓞ orcid.org/0000-0002-4034-724X; Email: marco.gobbi@ehu.eus

Luis E. Hueso − CIC nanoGUNE BRTA, 20018 Donostia-San Sebastián, Basque Country, Spain; IKERBASQUE, Basque Foundation for Science, 48009 Bilbao, Basque Country, Spain; ⓞ orcid.org/0000-0002-7918-8047; Email: l.hueso@nanogune.eu

Authors

Tanweer Ahmed − CIC nanoGUNE BRTA, 20018 Donostia-San Sebastián, Basque Country, Spain; ⓞ orcid.org/0000-0002-5921-8405

Bao Q. Tu − CIC nanoGUNE BRTA, 20018 Donostia-San Sebastián, Basque Country, Spain; ⓞ orcid.org/0000-0002-7857-400X

Eleni Chatzikyriakou − Centro de Física de Materiales CSIC-UPV/EHU, 20018 Donostia-San Sebastián, Basque Country, Spain

Lucía Olano-Vegas − CIC nanoGUNE BRTA, 20018 Donostia-San Sebastián, Basque Country, Spain

Beatriz Martín-García − CIC nanoGUNE BRTA, 20018 Donostia-San Sebastián, Basque Country, Spain; IKERBASQUE, Basque Foundation for Science, 48009 Bilbao, Basque Country, Spain

M. Reyes Calvo − BCMaterials, Basque Center for Materials, Applications and Nanostructures, 48940 Leioa, Spain; IKERBASQUE, Basque Foundation for Science, 48009 Bilbao, Basque Country, Spain; ⓞ orcid.org/0000-0001-5991-2619

Stepan S. Tsirkin − Centro de Física de Materiales CSIC-UPV/EHU, 20018 Donostia-San Sebastián, Basque Country, Spain; IKERBASQUE, Basque Foundation for Science, 48009 Bilbao, Basque Country, Spain

Ivo Souza − Centro de Física de Materiales CSIC-UPV/EHU, 20018 Donostia-San Sebastián, Basque Country, Spain; IKERBASQUE, Basque Foundation for Science, 48009 Bilbao, Basque Country, Spain

Félix Casanova − CIC nanoGUNE BRTA, 20018 Donostia-San Sebastián, Basque Country, Spain; IKERBASQUE, Basque Foundation for Science, 48009 Bilbao, Basque Country, Spain; ⓞ orcid.org/0000-0003-0316-2163

Fernando de Juan − IKERBASQUE, Basque Foundation for Science, 48009 Bilbao, Basque Country, Spain; Donostia International Physics Center, 20018 Donostia-San Sebastián, Basque Country, Spain

Complete contact information is available at:
https://pubs.acs.org/10.1021/acs.nanolett.4c03944

Author Contributions

M.R. and L.E.H. conceived and led the experimental work. M.R., T.A., B.Q.T., and L.O.-V. worked on the exfoliation of vdW materials. T.A. and B.Q.T. carried out device fabrication. M.R. and B.M.-G. contributed to the installation of the experimental photocurrent equipment. M.R. conducted photocurrent experiments, Raman spectroscopy, and electrical

ABBREVIATIONS

BPVE, bulk photovoltaic effect; CW, continuous wave; hBN, hexagonal boron nitride; vdW, van der Waals

REFERENCES

(1) Buscema, M.; Groenendijk, D. J.; Steele, G. A.; Van Der Zant, H. S.; Castellanos-Gomez, A. Photovoltaic effect in few-layer black phosphorus PN junctions defined by local electrostatic gating. *Nat. Commun.* **2014**, *5*, 4651.

(2) Furchi, M. M.; Pospischil, A.; Libisch, F.; Burgdorfer, J.; Mueller, T. Photovoltaic effect in an electrically tunable van der Waals heterojunction. *Nano Lett.* **2014**, *14*, 4785.

(3) Ramos, M.; Gadea, M.; Mañas-Valero, S.; Boix-Constant, C.; Henríquez-Guerra, E.; Díaz-García, M. A.; Coronado, E.; Calvo, M. R. Tunable, multifunctional opto-electrical response in multilayer FePS3/single-layer MoS2 van der Waals p-n heterojunctions. *Nanoscale Adv.* **2024**, *6*, 1909.

(4) Shockley, W.; Queisser, H. Detailed balance limit of efficiency of p-n junction solar cells. *J. Appl. Phys.* **1961**, *32*, 510.

(5) Aftab, S.; Iqbal, M. Z.; Haider, Z.; Iqbal, M. W.; Nazir, G.; Shehzad, M. A. Bulk Photovoltaic Effect in 2D Materials for Solar-Power Harvesting. *Adv. Opt. Mater.* **2022**, *10*, 2201288.

(6) Morimoto, T.; Nagaosa, N. Topological nature of nonlinear optical effects in solids. *Science Adv.* **2016**, *2*, No. e1501524.

(7) Cook, A. M.; Fregoso, B. M.; De Juan, F.; Coh, S.; Moore, J. E. Design principles for shift current photovoltaics. *Nat. Commun.* **2017**, *8*, 14176.

(8) Dai, Z.; Rappe, A. M. Recent progress in the theory of bulk photovoltaic effect. *Chem. Phys. Rev.* **2023**, *4*, 011303.

(9) Tan, L. Z.; Zheng, F.; Young, S. M.; Wang, F.; Liu, S.; Rappe, A. M. Shift current bulk photovoltaic effect in polar materials—hybrid and oxide perovskites and beyond. *npj Comput. Mater.* **2016**, *2*, 1.

(10) Koch, W. T.; Munser, R.; Ruppel, W.; Würfel, P. Bulk photovoltaic effect in BaTiO3. *Solid State Commun.* **1975**, *17*, 847.

(11) Glass, A. M.; Von der Linde, D.; Negran, T. J. High-voltage bulk photovoltaic effect and the photorefractive process in LiNbO3. *Appl. Phys. Lett.* **1974**, *25*, 233.

(12) Glass, A. M.; Von der Linde, D.; Auston, D. H.; Negran, T. J. Excited state polarization, bulk photovoltaic effect and the photo-refractive effect in electrically polarized media. *J. Electron. Mater.* **1975**, *4*, 915.

(13) Brody, P. S.; Crowne, F. Mechanism for the high voltage photovoltaic effect in ceramic ferroelectrics. *J. Electron. Mater.* **1975**, *4*, 955.

(14) Brody, P. S. High voltage photovoltaic effect in barium titanate and lead titanate-lead zirconate ceramics. *J. Solid State Chem.* **1975**, *12*, 193.

(15) Wang, M.; Wei, H.; Wu, Y.; Jia, J.; Yang, C.; Chen, Y.; Chen, X.; Cao, B. Polarization-enhanced bulk photovoltaic effect of BiFeO3 epitaxial film under standard solar illumination. *Phys. Lett. A* **2020**, *384*, 126831.

(16) Alexe, M.; Hesse, D. Tip-enhanced photovoltaic effects in bismuth ferrite. *Nat. Commun.* **2011**, *2*, 256.

(17) Nadupalli, S.; Kreisel, J.; Granzow, T. Increasing bulk photovoltaic current by strain tuning. *Science Adv.* **2019**, *5*, No. eaau9199.

(18) Ai, H.; Kong, Y.; Liu, D.; Li, F.; Geng, J.; Wang, S.; Lo, K. H.; Pan, H. 1T‴ transition-metal dichalcogenides: strong bulk photo-voltaic effect for enhanced solar-power harvesting. *J. Phys. Chem. C* **2020**, *124*, 11221.

(19) Schankler, A. M.; Gao, L.; Rappe, A. M. Large bulk piezophotovoltaic effect of monolayer 2 H-MoS2. *J. Phys. Chem. Lett.* **2021**, *12*, 1244.

(20) Akamatsu, T.; Ideue, T.; Zhou, L.; Dong, Y.; Kitamura, S.; Yoshii, M.; Yang, D.; Onga, M.; Nakagawa, Y.; Watanabe, K.; Taniguchi, T. A van der Waals interface that creates in-plane polarization and a spontaneous photovoltaic effect. *Science* **2021**, *372*, 68.

(21) Aftab, S.; Shehzad, M. A.; Salman Ajmal, H. M.; Kabir, F.; Iqbal, M. Z.; Al-Kahtani, A. A. Bulk photovoltaic effect in two-dimensional distorted MoTe2. *ACS Nano* **2023**, *17*, 17884.

(22) Jiang, J.; Chen, Z.; Hu, Y.; Xiang, Y.; Zhang, L.; Wang, Y.; Wang, G. C.; Shi, J. Flexo-photovoltaic effect in MoS2. *Nature Nanotechnol.* **2021**, *16*, 894.

(23) Aftab, S.; Iqbal, M. Z.; Iqbal, M. W.; Shehzad, M. A. Strain-enhanced photovoltaic effect in MoTe2. *Laser Photonics Rev.* **2023**, *17*, 2200429.

(24) Sun, R. X.; Hu, Z.; Zhao, X.; Zha, M. J.; Zhang, J.; Chen, X. D.; Liu, Z.; Tian, J. Strain-prompted giant flexo-photovoltaic effect in two-dimensional violet phosphorene nanosheets. *ACS Nano* **2024**, *18*, 13298.

(25) Xin, J.; Guo, Y. Bulk photovoltaic effect in the elemental blue phosphorus-based polar homojunction and heterojunction. *J. Phys. Chem. C* **2024**, *128*, 9705.

(26) Xie, X.; Leng, P.; Ding, Z.; Yang, J.; Yan, J.; Zhou, J.; Li, Z.; Ai, L.; Cao, X.; Jia, Z.; Zhang, Y. Surface photogalvanic effect in Ag2Te. *Nat. Commun.* **2024**, *15*, 5651.

(27) Quereda, J.; Ghiasi, T. S.; You, J. S.; van den Brink, J.; van Wees, B. J; van der Wal, C. H. Symmetry regimes for circular photocurrents in monolayer MoSe2. *Nat. Commun.* **2018**, *9*, 3346.

(28) Ma, Q.; Lui, C. H.; Song, J. C.; Lin, Y.; Kong, J. F.; Cao, Y.; Dinh, T. H.; Nair, N. L.; Fang, W.; Watanabe, K; Taniguchi, T. Giant

intrinsic photoresponse in pristine graphene. *Nat. Nanotechnol.* **2019**, *14*, 145.

(29) Yang, D.; Wu, J.; Zhou, B. T.; Liang, J.; Ideue, T.; Siu, T.; Awan, K. M.; Watanabe, K.; Taniguchi, T.; Iwasa, Y.; Franz, M. Spontaneous-polarization-induced photovoltaic effect in rhombohedrally stacked MoS2. *Nat. Photonics* **2022**, *16*, 469.

(30) Li, Y.; Fu, J.; Mao, X.; Chen, C.; Liu, H.; Gong, M.; Zeng, H. Enhanced bulk photovoltaic effect in two-dimensional ferroelectric CuInP2S6. *Nat. Commun.* **2021**, *12*, 5896.

(31) Chen, X.; Xu, K.; Qin, T.; Wang, Y.; Chen, Y.; Liu, H.; Xiong, Q. Bulk photovoltaic effect in two-dimensional ferroelectric semiconductor In2Se3. *arXiv* **2023**, 2308.08382.

(32) Yu, J.; Huang, B.; Yang, S.; Zhang, Y.; Bai, Y.; Song, C.; Ming, W.; Liu, W.; Wang, J.; Li, C.; Wang, Q. Flexoelectric Engineering of Bulk Photovoltaic Photodetector. *Nano Lett.* **2024**, *24*, 6337.

(33) Nahid, S. M.; Nam, S.; van der Zande, A. M. Depolarization field-induced photovoltaic effect in graphene/α-In2Se3/graphene heterostructures. *ACS Nano* **2024**, *18*, 14198.

(34) Wildervanck, J. C.; Jellinek, F. The dichalcogenides of technetium and rhenium. *J. Less-Common Met.* **1971**, *24*, 73.

(35) Lamfers, H. J.; Meetsma, A.; Wiegers, G. A.; De Boer, J. L. The crystal structure of some rhenium and technetium dichalcogenides. *J. Alloys Compd.* **1996**, *241*, 34.

(36) Rahman, M.; Davey, K.; Qiao, S. Z. Advent of 2D rhenium disulfide (ReS2): fundamentals to applications. *Adv. Funct. Mater.* **2017**, *27*, 1606129.

(37) Qiao, X. F.; Wu, J. B.; Zhou, L.; Qiao, J.; Shi, W.; Chen, T.; Zhang, X.; Zhang, J.; Ji, W.; Tan, P. H. Polytypism and unexpected strong interlayer coupling in two-dimensional layered ReS2. *Nanoscale* **2016**, *8*, 8324.

(38) Song, Y.; Hu, S.; Lin, M. L.; Gan, X.; Tan, P. H.; Zhao, J. Extraordinary second harmonic generation in ReS2 atomic crystals. *ACS Photonics* **2018**, *5*, 3485.

(39) Wan, Y.; Hu, T.; Mao, X.; Fu, J.; Yuan, K.; Song, Y.; Gan, X.; Xu, X.; Xue, M.; Cheng, X.; Huang, C. Room-temperature ferroelectricity in 1T′-ReS2 multilayers. *Phys. Rev. Lett.* **2022**, *128*, 067601.

(40) Zhou, Y.; Zhou, X.; Yu, X. L.; Liang, Z.; Zhao, X.; Wang, T.; Miao, J.; Chen, X. Giant intrinsic photovoltaic effect in one-dimensional van der Waals grain boundaries. *Nat. Commun.* **2024**, *15*, 501.

(41) Liang, Z.; Zhou, X.; Zhang, L.; Yu, X. L.; Lv, Y.; Song, X.; Zhou, Y.; Wang, H.; Wang, S.; Wang, T.; Shum, P. P. Strong bulk photovoltaic effect in engineered edge-embedded van der Waals structures. *Nat. Commun.* **2023**, *14*, 4230.

(42) Wang, J.; Han, N.; Lin, Z.; Hu, S.; Tian, R.; Zhang, M.; Zhang, Y.; Zhao, J.; Gan, X. A giant intrinsic photovoltaic effect in atomically thin ReS2. *Nanoscale* **2024**, *16*, 3101.

(43) Wang, W.; Xiao, Y.; Li, T.; Lu, X.; Xu, N.; Cao, Y. Piezo-photovoltaic Effect in Monolayer 2H-MoS2. *J. Phys. Chem. Lett.* **2024**, *15*, 3549.

(44) Dong, Y.; Yang, M. M.; Yoshii, M.; Matsuoka, S.; Kitamura, S.; Hasegawa, T.; Ogawa, N.; Morimoto, T.; Ideue, T.; Iwasa, Y. Giant bulk piezophotovoltaic effect in 3R-MoS2. *Nat. Nanotechnol.* **2023**, *18*, 36.

(45) Lin, Y. C.; Komsa, H. P.; Yeh, C. H.; Bjorkman, T.; Liang, Z. Y.; Ho, C. H.; Huang, Y. S.; Chiu, P. W.; Krasheninnikov, A. V.; Suenaga, K. Single-layer ReS2: two-dimensional semiconductor with tunable in-plane anisotropy. *ACS Nano* **2015**, *9*, 11249.

(46) Intonti, K.; Faella, E.; Kumar, A.; Viscardi, L.; Giubileo, F.; Martucciello, N.; Lam, H. T.; Anastasiou, K.; Craciun, M.; Russo, S.; Di Bartolomeo, A. Temperature-dependent conduction and photoresponse in few-layer ReS2. *ACS Appl. Mater. Inter.* **2023**, *15*, 50302.

(47) Park, J. Y.; Joe, H. E.; Yoon, H. S.; Yoo, S.; Kim, T.; Kang, K.; Min, B. K.; Jun, S. C. Contact effect of ReS2/metal interface. *ACS Appl. Mater. Inter.* **2017**, *9*, 26325.

(48) Akatsuka, S.; Sakano, M.; Yamamoto, T.; Nomoto, T.; Arita, R.; Murata, R.; Sasagawa, T.; Watanabe, K.; Taniguchi, T.; Mitsuishi, N.; Kitamura, M. 180°-twisted bilayer ReSe2 as an artificial non-centrosymmetric semiconductor. *Phys. Rev. Res.* **2024**, *6*, L022048.

(49) Ibañez-Azpiroz, J.; Tsirkin, S. S.; Souza, I. Ab initio calculation of the shift photocurrent by Wannier interpolation. *Phys. Rev. B* **2018**, *97*, 245143.